Materials Science & Engineering A 838 (2022) 142743

Contents lists available at ScienceDirect

Materials Science & Engineering A

journal homepage: www.elsevier.com/locate/msea

The strain rate sensitive flow stresses and constitutive equations of a selective-laser-melt and an annealed-rolled 316L stainless steel: A comparative study

Mustafa Güden [a,*], Samed Enser [a], Mesut Bayhan [a], Alper Taşdemirci [a], Hakan Yavaş [b]

[a] Dynamic Testing and Modelling Laboratory, İzmir Institute of Technology, İzmir, Turkey
[b] Turkish Aerospace Industries, Additive Manufacturing Technology Center, Kahramankazan, Ankara, Turkey

ARTICLE INFO

Keywords:
Selective-laser-melt 316L
Annealed-rolled 316L
Strain rate sensitivity
Compressive flow stress
Flow stress equations
Twinning and deformation martensite

ABSTRACT

The strain rate dependent compressive flow stresses of a Selective-Laser-Melt 316L (SLM-316L) alloy and a commercial (annealed-extruded) 316L (C-316L) alloy were determined, for comparison, between $1x10^{-4}$ and ~2500 s^{-1} and between $1x10^{-4}$ and ~2800 s^{-1}, respectively. The Johnson and Cook flow stress material model parameters of both alloys were also determined. The microstructural examinations of the deformed cross-sections of tested specimens (interrupted tests) showed a twinning-induced-plasticity in SLM-316L alloy and a martensitic transformation-induced-plasticity in C-316L alloy. Twin and martensite formations were detected microscopically higher in the dynamically tested specimens until about 0.22 strain, while the twin and martensite formations decreased at increasing strains due to adiabatic heating. The rate sensitivity of SLM-316L was determined slightly higher than that of C-316L within the quasi-static strain rate range ($1x10^{-4}$ and $1x10^{-2}$ s^{-1}), while the rate sensitivities of both alloys were similar in the quasi-static-high strain rate range ($1x10^{-4}$ and ~2500-2800 s^{-1}) at low strains. A more rapid decrease in the rate sensitivity of C-316L at increasing strains was found in the quasi-static-high strain rate range. The similar activation volumes of both alloys, corresponding to the dislocation intersections, indicated a similar thermally activated deformation process involvement in both alloys.

1. Introduction

The microstructure of metal additive Selective-Laser-Melt 316L (SLM-316L) alloy exhibits columnar grains (parallel to the laser building direction) and the micro/nano size sub-grain or sub-cell (intercellular structure) inside larger grains [1–11]. These sub-grains are formed by the dislocation networks and contain heavy atoms, Cr and Mo [1,12]. Also, a crystallographic fiber texture in which <100> directions were aligned in the build direction was commonly reported, while the texture was altered into <110> and <111> directions by reducing hatching spacing and by increasing laser power [10,13–17]. Rotating scanning; however, induced a ⟨110⟩ fiber texture in the build direction and a near-random crystallographic orientation in the transverse to the build direction [18]. Furthermore, SLM-316L alloy is deformed by a twin-induced-plasticity (TWIP) [7,9,10,19] with an increased yield strength as compared with conventional 316L (C-316L) alloys [9,12,20]. The yield strengths of SLM-316L and C-316L alloys at quasi-static strain rates ranged 450–590 MPa and 160–365 MPa, respectively [21]. The increased yield strength of SLM-316L is ascribed to relatively high dislocation densities, $>1x10^{15}$ m^{-2} [9,22,23]. Although the quasi-static mechanical properties and deformation mechanisms of SLM-316L have been widely investigated and well clarified, there have been few studies on the deformation response at increasing strain rates as will be explained below.

As a benchmark, the mechanical response of C-316L alloy at increasing strain rates will be outlined here. In an early study in 1985, a nuclear grade 316H specimens were plastically pre-strained and unloaded at 0.004 s^{-1}, then reloaded at 500 s^{-1} in a tension Split Hopkinson Pressure Bar (SHPB) [24]. The material showed a moderate strain-rate sensitive flow stress behavior without any strain-rate-history effect. A strain rate sensitive tensile flow stress behavior was reported for a C-316L alloy between 0.02 and ~100 s^{-1} [25]. Adiabatic shear localization in an annealed-rolled C-316L alloy was investigated using an SHPB and hat-shaped specimens [26,27]. The annealed alloy exhibited a substantial work hardening and adiabatic shear band formation following the peak shear stress. The compression flow stresses of

* Corresponding author.
E-mail address: mustafaguden@iyte.edu.tr (M. Güden).

https://doi.org/10.1016/j.msea.2022.142743
Received 20 November 2021; Received in revised form 26 January 2022; Accepted 27 January 2022
Available online 29 January 2022

a sintered 316L alloy from 10^{-3} to $7.5x10^{3}$ s^{-1} [28] and a biomedical grade 316L alloy from $1x10^{3}$ s^{-1} to 5 10^{3} s^{-1} were determined between 25 and 800 °C [29,30]. The compressive flow stress of the sintered alloy increased with increasing strain rate from quasi-static to dynamic strain rates, while an increased strain rate sensitivity was found in the dynamic strain rate range after about $3x10^{3}$ s^{-1} [28]. The flow stress and work-hardening rate of the biomedical 316L alloy increased with increasing strain rate but decreased with increasing temperature [29, 30]. The strain rate sensitive flow stresses of C-316L alloy were also reported in other studies [31–33].

There have been however few studies on the strain rate sensitive flow stress behavior of SLM-316L alloy. The strain rate sensitivity of a laser-melt-deposited 316L was determined between $1x10^{-3}$ and 1 s^{-1} in tension [34]. The laser melt deposited 316L alloy was reported to exhibit a higher strain rate sensitive flow stresses than C-316L alloy. A similar result was also reported in Ref. [35] in which the tensile flow stress strain rate sensitivity of SLM-316L alloy was found to be higher than that of C-316L alloy between $5x10^{-5}$ and $1x10^{-1}$ s^{-1}. The increased rate sensitivity of SLM-316L as compared with C-316-L was reported, in the same study, due to the reduced deformation activation volume of SLM-316L. A recent study performed under compression at quasi-static and high strain rates (up to ~2000 s^{-1}) however has shown a contradicting result with above studies: SLM-316L alloy exhibited a lower strain rate sensitivity than C-316L alloy [36].

As a continuation of the above studies, present study investigates the strain rate sensitivity and deformation microstructure of an SLM-316L alloy under compression at quasi-static strain rates, 10^{-4}-10^{-2} s^{-1}, and between quasi-static and high strain rate, ~2500 s^{-1}. For comparison, a commercially available annealed-extruded C-316L alloy was also tested at 10^{-4}-10^{-2} s^{-1} and ~2800 s^{-1}. The compression test specimens of SLM-316L were tested normal to the SLM building direction and the C-316L specimens through the extrusion direction. In a previous study [37], the rate sensitivities and deformation microstructures of both SLM-316L and C-316L alloys were investigated in the quasi-static strain rate range, between $1x10^{-4}$ and $1x10^{-2}$ s^{-1}. In present study, the strain rate range was extended to high strain rates, the constitutive equations of both alloys were determined and additionally interrupted tests at high strain rates were performed in order to analyze the deformation microstructure development as functions of strain and strain rate. The XRD measurements on the untested specimens and the specimens tested until about a prescribed strains were made in order to determine crystal phases in both alloys.

2. Materials and methods

2.1. Sample preparation

The test specimens for the compression tests were extracted from the rectangular SLM-316L bars fabricated in a Laser-powder bed fusion AM Concept Laser M2 Cusing device using nitrogen gas as a protective atmosphere. The bars were fabricated using a gas atomized 316L powder with a mean powder diameter of 50 μm. The following process parameters were used in the SLM: the power = 370 W, the scanning rate = 900 mm s^{-1}, the hatching space = 115 μm and the spot size of the incident beam = 160 μm. A biaxial scanning in which the laser pattern was rotated 90° between adjacent layers (Fig. 1(a)) with an energy density of ~120 J mm^{-3} and a 30 μm constant layer thickness was used to construct the samples. The used axis notation is as follows: the building direction is the z-axis and the directions normal to the melt pools in the biaxial plane are the x- and y-axis as shown in Fig. 1(b). It is also seen in Fig. 1 (b) that melt pools appear as overlapping semi ellipse rather than nail-tops due to the used rotating scanning strategy.

Quasi-static and high strain rate cylindrical compression test specimens were machined from a 6x13x130 mm as-built rectangular bar shown in Fig. 2(a). After removing the support (bottom of the bar) and machining 0.5 mm from each side of the bar, the compression test specimens, 5 mm in diameter and 5 mm in length were cut using an electro-discharge machine (Fig. 2(a)). The compression tests were conducted parallel to the biaxial plane in the x-direction, as shown in Fig. 2 (a). In order to determine the homogeneous mechanical properties along the SLM-built bar, hardness tests were performed from the bottom (support) to the top of the bar. The hardness profile in Fig. 2(b) indicates that at a distance above 25 mm from the bottom, the average hardness values become homogenous along the bar. Therefore, the compression tests specimens were prepared 25 mm away from the bottom of the bar. Cylindrical samples of an annealed extruded-316 L alloy bar of Viraj Impoexpo (5 mm in diameter and 5 mm in length) were also prepared using the same method. The major alloy compositions of the used SLM powder and C-316L are listed in Table 1.

Samples for metallographic analyses were prepared in a precision diamond saw under a continuous flow of water. Bakelite-mounted samples were then ground and polished using diamond suspensions and then etched by a solution of 10% HNO_3, 20% HCl and 20% Glycerol. Microscopic analyses were performed in a Meiji IM7 100 optical microscope and a FEI Quanta 205 FEG and Philips XL 30SFEG scanning electron microscope. The crystallographic structures of untested and compression tested specimens were determined using a Philips X'Pert Pro X-Ray Diffraction (XRD) device (Cu-Kα radiation, λ = 1.54 A° and 40 kV). Vickers Hardness (HV) tests were conducted on the polished and polished-etched surfaces of metallographic samples in a Shimadzu Micro Vickers Hardness Tester by applying 19.61 N loads for 10 ms (10 repeating tests). The density and porosity level of the used SLM-316L were given elsewhere [22], and 7821 ± 5 kg m^{-3} and 0.22%, respectively. The porosity level is comparable with the reported density of an SLM316-L alloy using the similar processing parameters [35]. The porosities of SLM316-L alloys processed using different scanning strategies are also noted generally less than one percent [38].

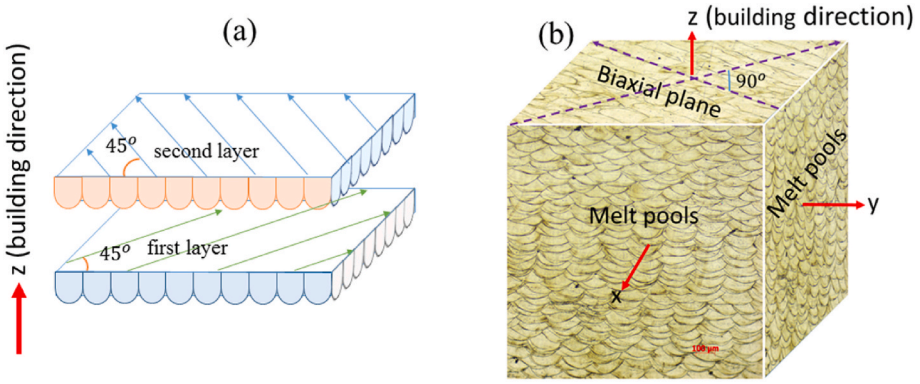

Fig. 1. The schematic of (a) the rotating scanning between adjacent layers and (b) melt pools and directions, x-, y- and z-axis.

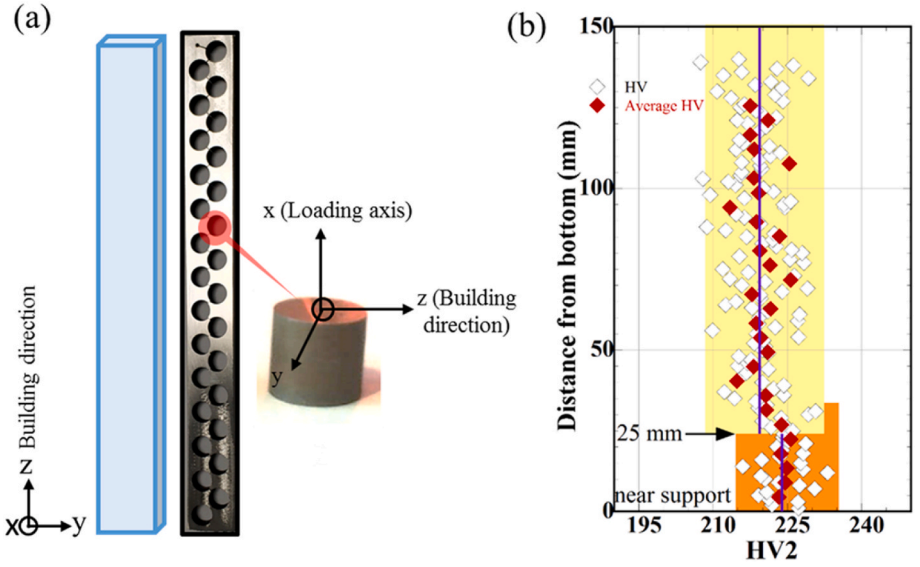

Fig. 2. (a) The schematic and picture of as-built SLM-316L bar and the picture of an extracted cylindrical compression tests specimen showing the loading direction and (b) hardness and average hardness variations along the bar height.

Table 1
The chemical compositions of the SLM powder and C-316L

	C	Mn	Si	Ni	Cr	Mo	N
SLM	<0.03			10.0–13.0	16.5–18.5	2.0–2.5	
C-316L	0.022	1.40	0.45	10.04	16.30	2.05	0.069

2.2. Quasi-static and high strain rate tests

Quasi-static compression tests were performed at three different strain rates, $1x10^{-4}$, $1x10^{-3}$ and $1x10^{-2}$ s^{-1}, in a Shimadzu test machine using a video extensometer and high strain rate compression tests were performed in an SHPB test apparatus. Interrupted tests at quasi-static and high strain rate were performed until about predetermined engineering strains in order to determine the deformation microstructure development as functions of strain and strain rate. In these tests, test specimens were inserted inside tool-steel rings having a 19 mm outer and a 10 mm inner diameter with 4.5, 4, 3.5 and 3 mm thicknesses corresponding to the final engineering strains of 0.1, 0.2, 0.3 and 0.4 engineering strains (0.11, 0.22, 0.36 and 0.51 true strains) in the test specimens, respectively. When the ring was compressed together with the specimen, the force values increased abruptly; thereafter, the test was stopped.

The schematic of the used SHPB set-up is shown in Fig. 3(a). The SHPB set-up consisted of a 19.40 mm diameter Inconel 718 bar; 2000 mm-long incident bar, 1800 mm-long transmitter bar and 50 mm-long striker bar. The modulus and density of the bar are sequentially 204 GPa and 8394 kg m^{-3}. In order to not to damage the bar-end surfaces, impedance matched 5 mm-thick tool steel inserts were used at the bar ends. Initial tests were performed on an Al alloy with and without using inserts to check any artificial wave reverberations from the inserts. Both ended with the same stress-strain behavior. The stresses on the bars were measured by a full Wheatstone-bridge configuration of 350 Ω foil strain gages. After recording the waves using an oscilloscope and amplifier, the strain (ε_s), stress (σ_s) and strain rate ($\dot{\varepsilon}_s$) of the sample were using the following relations

$$\varepsilon_s(t) = -\frac{2C_b}{L_s}\int_0^t \varepsilon_R(t)dt \tag{1}$$

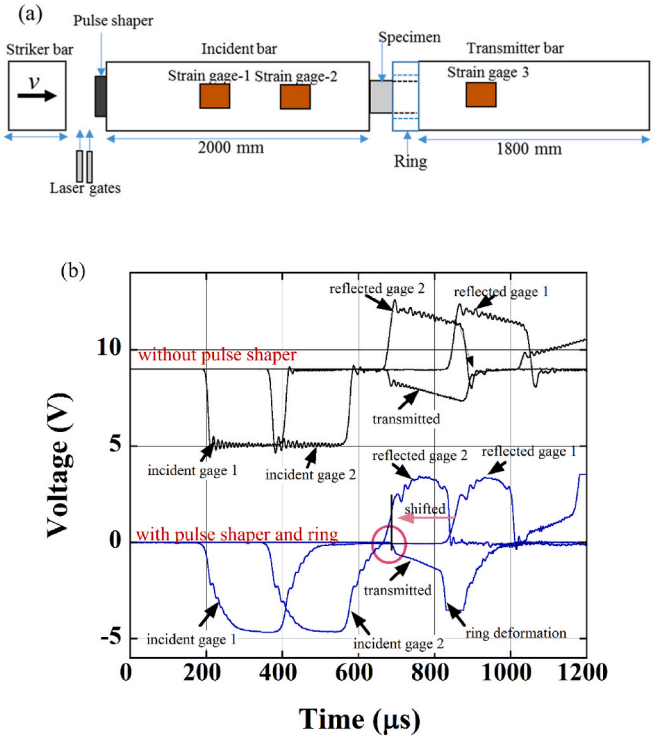

Fig. 3. (a) The schematic of the SHPB test set-up and (b) incident, transmitter and reflected wave voltage reading without pulse shape and with pulse shaper and constraining ring.

$$\sigma_s(t) = \frac{A_b}{A_s}E_b\varepsilon_T(t) \tag{2}$$

$$\dot{\varepsilon}_s(t) = -\frac{2C_b}{L_s}\varepsilon_R(t) \tag{3}$$

where L_s, A_b, A_s, E_b, C_b and t are the specimen length, the bar cross-sectional area, the specimen cross-sectional area, the bar elastic modulus, the bar elastic wave velocity and the time, respectively. ε_R and ε_T are sequentially the reflected and transmitted strains. The SHPB pulse

shaping is widely used in order to induce a gradually-rising incident wave [39,40]. In this method, a thin layer of a ductile metal sheet is placed at the front of the incident bar so that the deformation of the metal sheet in between the striker and incident bar shapes the incoming incident bar stress. In the present study, a copper sheet in 10x10x1 mm size was placed at the front of the incident bar by applying a thin layer of lubricant. Fig. 3(b) shows typical voltage-time readings of the SHPB test without and with using a pulse shaper and a constraining ring. As is seen in the figure, the pulse-shaper induces, a more gradually-rising stress wave on the incident bar and also results in lesser variations of strain rate during a test. In classical SHPB tests, the strain gages on the incident and transmitter bars are placed at an equal distance from the specimen/bar interfaces so that the reflected and transmitter waves start at the same point on the time axis. The use of pulse shaper however increases the time duration of the incident wave, resulting in an interaction between the end of the incident wave and the start of the reflected wave (shown by a circle in Fig. 3(b)). A strain gage (strain gage 1 in Fig. 3(a)) was mounted on the incident bar to measure the incident and reflected waves separately. In this case, the strain gage 1 reading was shifted on the time axis until the reflected and transmitted waves started at the same point in the time domain. The use of two strain gages on the incident bar of the used SHPB also allows measuring the wave dispersion. The similar wave profiles measured from two strain gages show negligible dispersion in the Inconel bars.

In the interrupted high strain rate tests, after the specimen is compressed until about the predetermined strain, the ring and specimen are deformed together as depicted in Fig. 3(b). Due to the high mechanical impedance of the tool steel ring, the specimen is elastically deformed when it is compressed together with the tool steel ring. As soon as the ring is compressed as seen in Fig. 3(b), the reflected wave becomes zero and the incoming wave is fully transmitted to the transmitter bar. By this way, the specimen was deformed until about 0.11, 0.22, 0.36 and 0.51 true strains in the SHPB tests.

3. Results

3.1. Microstructural characterization and hardness

The optical and SEM micrographs of the untested SLM-316L parallel to the biaxial plane are shown in Fig. 4(a). A crystallographic fiber texture of ⟨110⟩ in the build direction (z-axis) and a random distribution of ⟨100⟩, ⟨110⟩ and ⟨111⟩ directions transverse to the build direction (x- and y-axis, ±45° to the scanning directions) were previously shown for the investigated SLM-316L [22]. Rotating scanning breaks the epitaxy of columnar growth [18]. The broken columnar grains of the studied SLM-316L alloy are shown by dotted lines across the melt pools in Fig. 4 (a). The average width of these broken grains were determined 29.27 ± 4.4 μm by linear intercept method. A cellular microstructure/sub-structure inside the grains is seen in the inset of Fig. 4(a). The widths of the cells were ranged 0.7–1.67 μm. The optical micrographs of the grain structure of commercial annealed-extruded 316-L are shown in Fig. 4(b). The typical polygonal equiaxed austenite grains are also seen in these figures. The average grain size measured 24.3 ± 3.22 μm by the same linear intercept method. The measured mean hardness values in the x-axis (tip normal to x-axis) and in the z-axis of SLM-316L are **220 ± 9** HV and 215 ± 7.6 HV, respectively. The mean hardness value of extruded C-316L was found lower than x- and z-axis of SLM-316L and 211 ± 6 HV.

3.2. Quasi-static and high strain rate compression behavior

Compression stress-strain curves of the investigated alloys were previously determined at $1x10^{-4}$, $1x10^{-3}$, and $1x10^{-2}$ s^{-1} and reported in Ref. [37]. The strain rate jump tests at $1x10^{-4}$, $1x10^{-3}$, and $1x10^{-2}$ s^{-1} were also performed in the same study, which provided a higher stress rise in SLM-316L. The average yield strengths (proof strength) were determined 510 ± 10.2 and 360 ± 11.6 MPa sequentially for SLM-316L and C-316L.

The representative compression true stress-true strain curves and true strain rate–true strain curves of both alloys are shown in Fig. 5(a). Since the high strain rate SHPB tests on both alloys were performed at the same gas-gun pressure (the same incident stress), softer C-316L exhibited higher strain rates as seen in Fig. 5(a). The strain rate is not constant in the SHPB tests and varies between 2500 and 3150 s^{-1} for SLM-316L and between 2800 and 3250 s^{-1} for C-316L, between 0.1 and 0.4 true strain (Fig. 5(a)). Fig. 5(b) shows the true-stress-true strain curves of SLM-316L at quasi-static and dynamic strain rates (three tests at each strain rate). In the high strain rate tests (2500-3150 s^{-1}), the sudden increase of stress is due to a higher mechanical impedance of the ring deformation after a predetermined strain, as marked in Fig. 5(b). Not shown here, similar interrupted tests were also performed at $1x10^{-3}$ s^{-1}. Fig. 5(c) shows the true-stress-true strain curves of C-316L at quasi-static and dynamic strain rates. Note that SHPB tests result in large stress oscillations at the beginning of stress-strain curves, partly due to the geometrical artifacts induced by the specimen-bar contacts and partly due to the non-equilibrium stress condition at these initial strains [41,42]. Nevertheless, it is clearly seen in Fig. 5(b) and (c), both alloys show a strain rate sensitive flow stress behavior: as the strain rate increases from quasi-static to high strain rate, the flow stress increases.

The work hardening (WH) of both alloys at quasi-static and high strain rates are shown in Fig. 6 together with the corresponding true stress-strain curves. The quasi-static WH of C-316L is seen higher than that of SLM-316L (Fig. 6). The quasi-static WH of both alloys maybe considered in three deformation regions. These regions corresponded to a rapidly reduced WH region at about 0.07 strain (I), a more slowly reduced WH region between 0.07 and 0.27 strain (II) and again a rapidly reduced WH region at the strains above 0.3 (III). Although the dynamic WH in C-316L is higher than the quasi-static HW at low strains, both

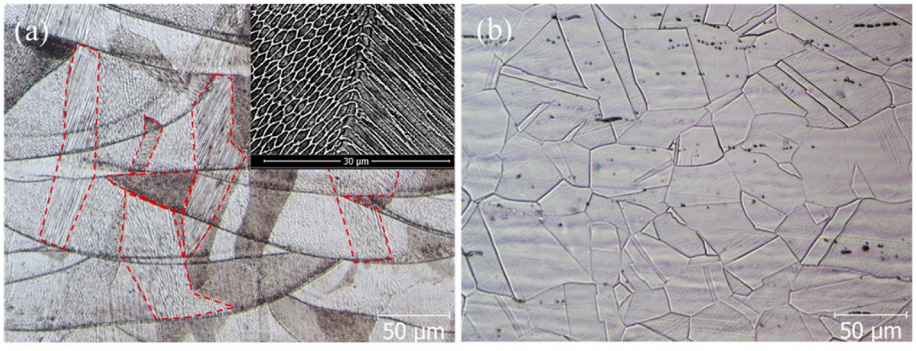

Fig. 4. The micrographs showing (a) the microstructure parallel to biaxial plane of SLM-316L and the sub-grain structure (b) the microstructure of C-316L normal to extrusion direction.

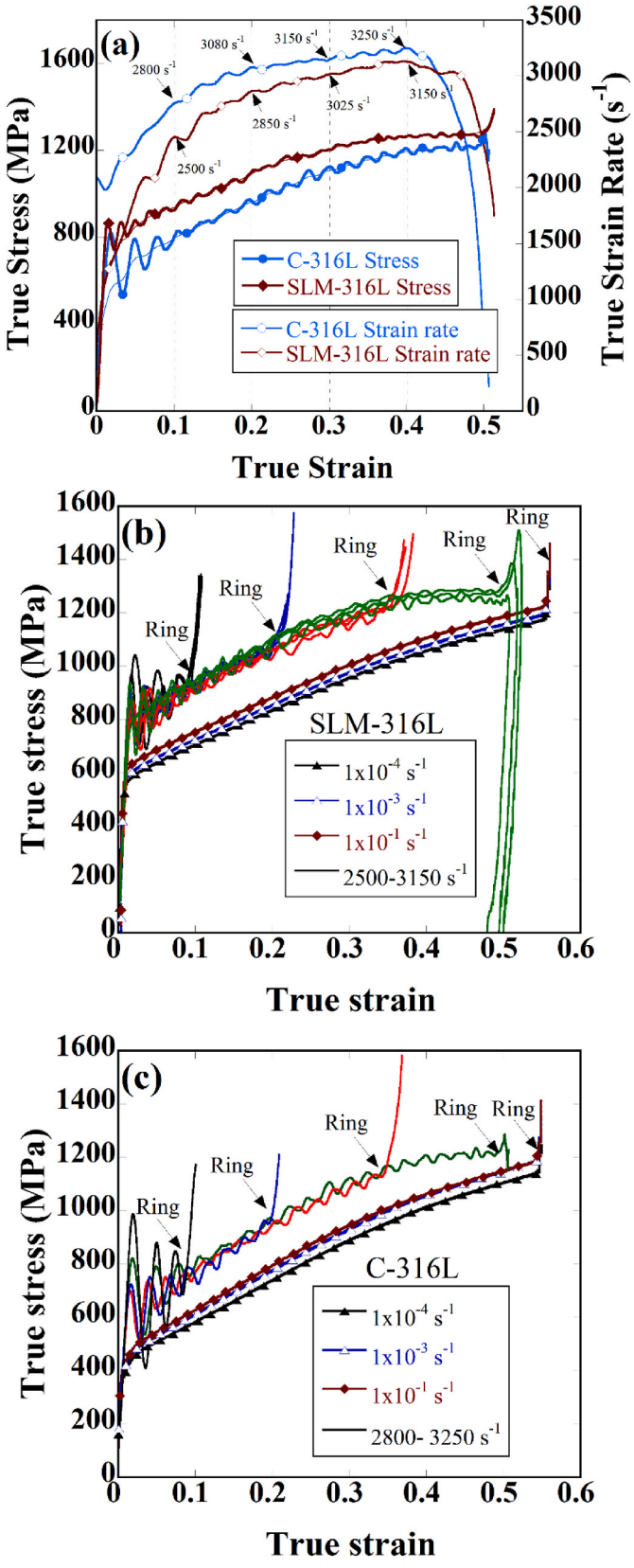

Fig. 5. (a) True stress and true strain curves in SHPB tests, (b) true stress-true strain curves of (b) SLM-316L and (c) C-316L at quasi-static and dynamic strains rates.

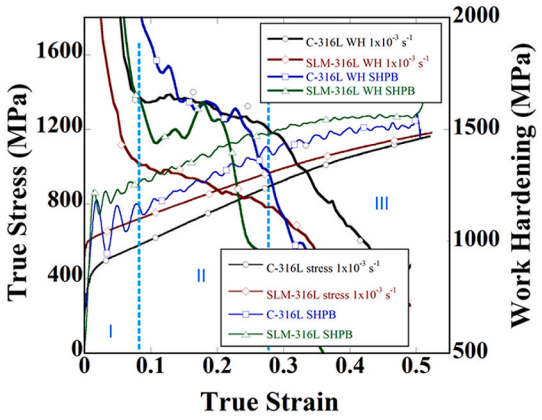

Fig. 6. Representative work hardening-true strain curves of SLM-316L and C-316L with quasi-static and high strain rate true stress-true strain curves and three distinct regions.

become equal to each other between 0.14 and 0.23 strain. After 0.23 strain, the dynamic WH decreases rapidly below the quasi-static WH. However, the dynamic WH of SLM-316L alloy is higher than the quasi-static HW until about 0.23 strain as seen in Fig. 6. The dynamic WH of SLM-316 alloy also reaches the quasi-static and dynamic HW of C-316L at about 0.18 strain. The rapid reduction of the dynamic WH of both alloys as compared with the quasi-static WH after about 0.20–0.23 strain is due to the adiabatic heating of the dynamically tested specimens, which reduces the deformation resistance. It is also noted that dynamic loading decreases the extent of region II. In the WH curves of the quasi-static loading of the same alloys, the region I is considered as the slip dominated, the region II as the twinning and/or martensite transformation-induced slip deformation dominated, and the region III as the slip dominated [37]. The twinning-dominated deformation of SLM-316L and the martensite transformation-dominated deformation of C-316L start at about 0.07 strain and continue until about ~0.3 strain.

3.3. Constitutive relations and strain rate sensitivity

The flow stresses of both alloys were fitted with the Johnson and Cook (JC) flow stress equation given as [43].

$$\sigma = (A + B\varepsilon^{n})\left[1 + c\ln\left(\frac{\dot{\varepsilon}}{\dot{\varepsilon}_{o}}\right)\right]\left(1 - \left[\frac{T - T_{r}}{T_{m} - T_{r}}\right]^{m}\right) \quad (4)$$

where, σ and ε are the equivalent true stress and true plastic strain, respectively. A, B, n, c and m are the JC parameters; n is the strain hardening coefficient, c is the strain rate sensitivity, T is the deformation temperature, T_r is the reference temperature, T_m is the melting temperature, m is the thermal softening parameter, and $\dot{\varepsilon}$ and $\dot{\varepsilon}_o$ are sequentially the strain rate and reference strain rate ($1x10^{-3}$ s^{-1}). Eqn. (4) is modified by replacing $(A + B\varepsilon^{n})$ with the stress-strain curve $(\sigma_o(\varepsilon))$. The values of $\sigma_o(\varepsilon)$ were determined by interpolating the experimental true stresses with true strain at $1x10^{-3}$ s^{-1}. To calculate the strain rate sensitivity parameter c, the true flow stresses at 0.11, 0.22, 0.36 and 0.51 strains are drawn against the logarithm of true strain rate and then the true flow stresses are fitted with Eqn. (4) as shown in Fig. 7(a) and (b), sequentially for SLM-316L and C-316L. The c values of SLM-316L decreases from 0.18 to 0.011 when the true strain increases from 0.11 to 0.56, as seen in Fig. 7(a). A similar reduction of the c values is also seen in C-316L within the same strain range, from 0.0185 to 0.009 (Fig. 7(b)). Different from SLM-316L, the c values of C316L decrease from 0.0185 to 0.0155 sequentially at 0.11 and 0.22 strain to a value of 0.013 when the flow stress is fitted between $1x10^{-4}$ s^{-1} and $1x10^{-2}$ s^{-1} as tabulated in the table in Fig. 7(b). The relatively lower c values of both alloys at increasing strains are partly due to the increased extent of adiabatic heating at increasing strains. The rate sensitivity parameters of

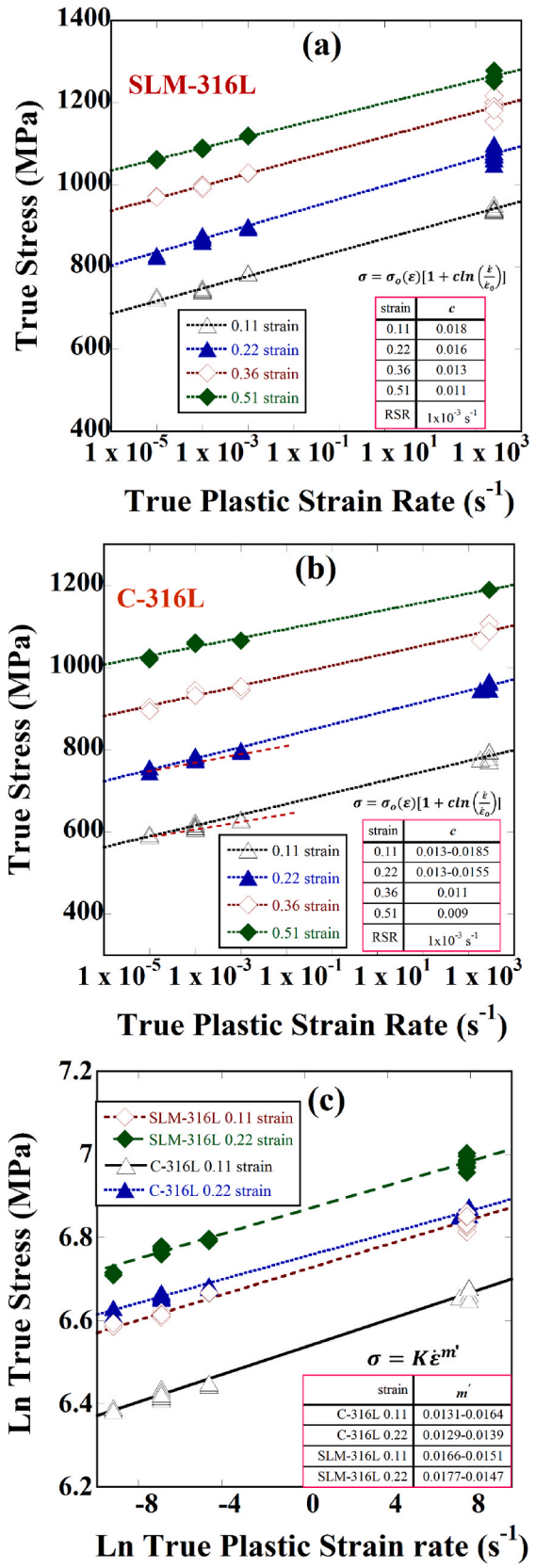

Fig. 7. The true stress vs. ln true plastic strain rate at different strains and the variation of c value with strain and strain rate (a) SLM-316L and (b) C-316L and (c) ln true stress vs. ln true plastic strain rate and m' values at different strains for SLM-316L and C-316L.

SLM-316L and C-316L as tabulated in Fig. 7(a) and (b) are very similar to each other at low strains, 0.11 and 0.22, while at increasing strains the rate sensitivity of SLM-316 becomes slightly higher than that of C-316L. In the quasi-static strain rate range; however, the rate sensitivity of SLM-316 is higher than that of C-316L. For comparison, the data in Fig. 7(a) and (b) were also fitted with the following relation [44],

$$\sigma = K\dot{\varepsilon}^{m'} \tag{5}$$

where K is a constant and m' is the strain rate sensitivity parameter, which is

$$m' = \left.\frac{d\ ln(\sigma)}{d\ \ln(\varepsilon)}\right|_{T,\varepsilon} \tag{6}$$

The fitting results of the flow stress data with Eqn. (5) are shown in Fig. 7(c) for SLM-316L and C-316L at 0.11 and 0.22 strain, respectively. The m' values are tabulated sequentially within the quasi-static strain rate range ($1x10^{-4}$-$1x10^{-2}$ s^{-1}) and within the quasi-static-high strain rate range ($1x10^{-4}$- up to 3150 and 3250 s^{-1}) in the same figure. The m' values of SLM-316L and C-316L are also very similar as seen in Fig. 7(c); for SLM-316L ranging 0.0166–0.051 at 0.11 strain and 0.0177–0.0147 at 0.22 strain and for C-316L ranging 0.0131–0.0164 at 0.11 strain and 0.0129–0.0139 at 0.22 strain. Again, SLM-316 shows a higher m' value in the quasi-static strain rate range.

The c parameters of SLM-316L and C316-L were fitted with true strain into a polynomial equation, as shown in Fig. 8(a). As noted in the same figure, the c parameters of both alloys are almost the same at 0.11 strain, while at increasing strains a more rapid decrease is seen in the c parameter of C-316L. The temperature softening parameter (m) of both alloys were determined by fitting the quasi-static compression yield strengths (taken from the literature) with the flowing relation: $\sigma = \sigma_r\left(1 - \left[\frac{T-T_r}{T_m-T_r}\right]^m\right)$, where σ_r is the room temperature yield strength. As is seen in Fig. 8(b), taking the m value equals to 1 for both alloys, results in a good match with the strength-temperature curves.

The predicted JC and experimental true stress-true strain curves at quasi-static strain rates ($1x10^{-4}$ and $1x10^{-2}$ s^{-1}) and high strain rate (SHPB) are shown Fig. 9(a) and (b) for SLM-316L and C-316L, respectively. Using the determined c values, the adiabatic stress-strain curves were predicted by taking $T = T_r$, while the isothermal curves were calculated using the following equation by taking $m = 1$,

$$\sigma = \frac{(A + B\varepsilon^n)\left[1 + cln\left(\frac{\dot{\varepsilon}}{\dot{\varepsilon}_o}\right)\right]}{\left(1 - \left[\frac{T-T_r}{T_m-T_r}\right]^m\right)} \tag{7}$$

In the same curves in Fig. 9(a) and (b), the temperature rise (ΔT) was calculated using the flowing relation,

$$\Delta T = \frac{\beta \int \sigma d\varepsilon}{\rho c_p} \tag{8}$$

where β and c_p are the Taylor–Quinney coefficient [46] (fraction of deformation work converted into heat) and the heat capacity, respectively. For both alloys, the value of c_p was taken 500 J kg^{-1} K^{-1} [47] and T_m = 1425 °C. The value of β for a cold rolled 316L specimen was reported below 0.9 and increased with increasing strain [48]. The measured β values of some metals and alloys have shown to depend on the testing type [49]. For example, the value was found higher in compression (0.7–0.9) than in tension for a CP-Ti. It was claimed that the formation of twin boundaries stored less amount of deformation energy; therefore, the value of β was higher in the compression tested specimen due to larger fractions of twinning deformation. As will be explained later, the tested SLM-316L deforms under compression by the TWIP and C-316L by the transformation-induced-plasticity (TRIP). Therefore, the value of β was taken 0.8 as an average for both alloys. The

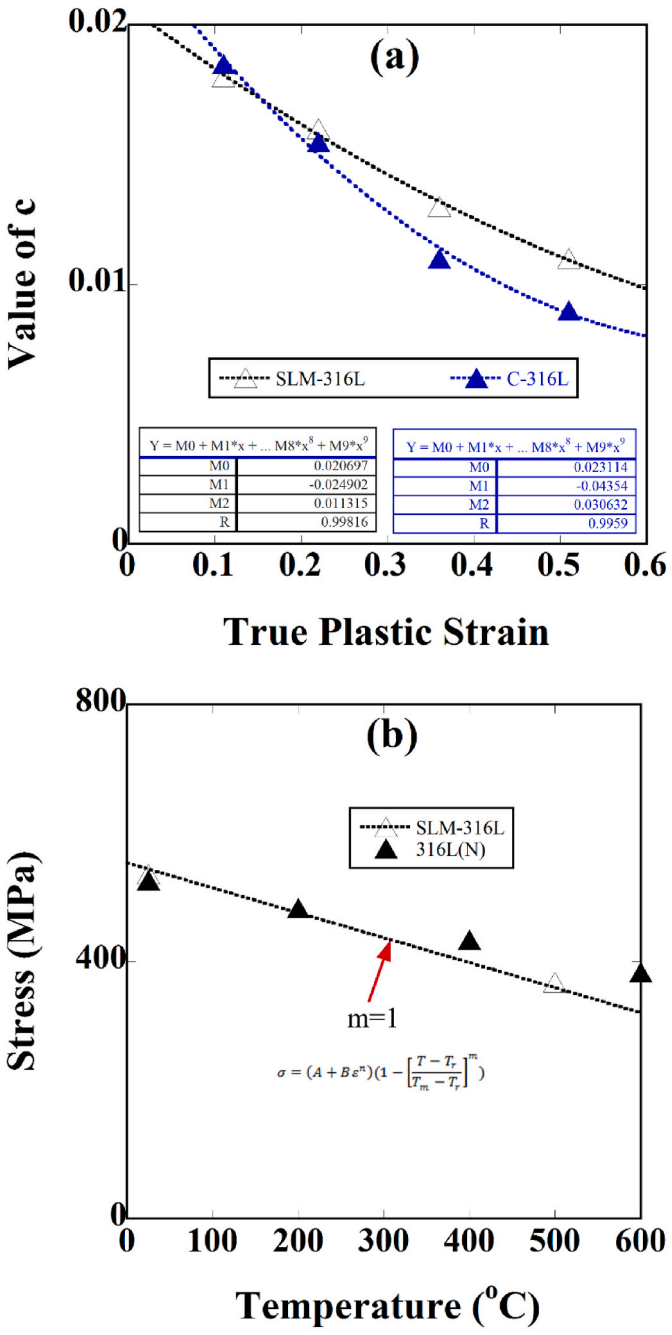

Fig. 8. The fitted value of (a) c with strain and (b) compression stress vs. temperature and fitted curve when $m = 1$, for SLM-316L and C-316L ([30,45]).

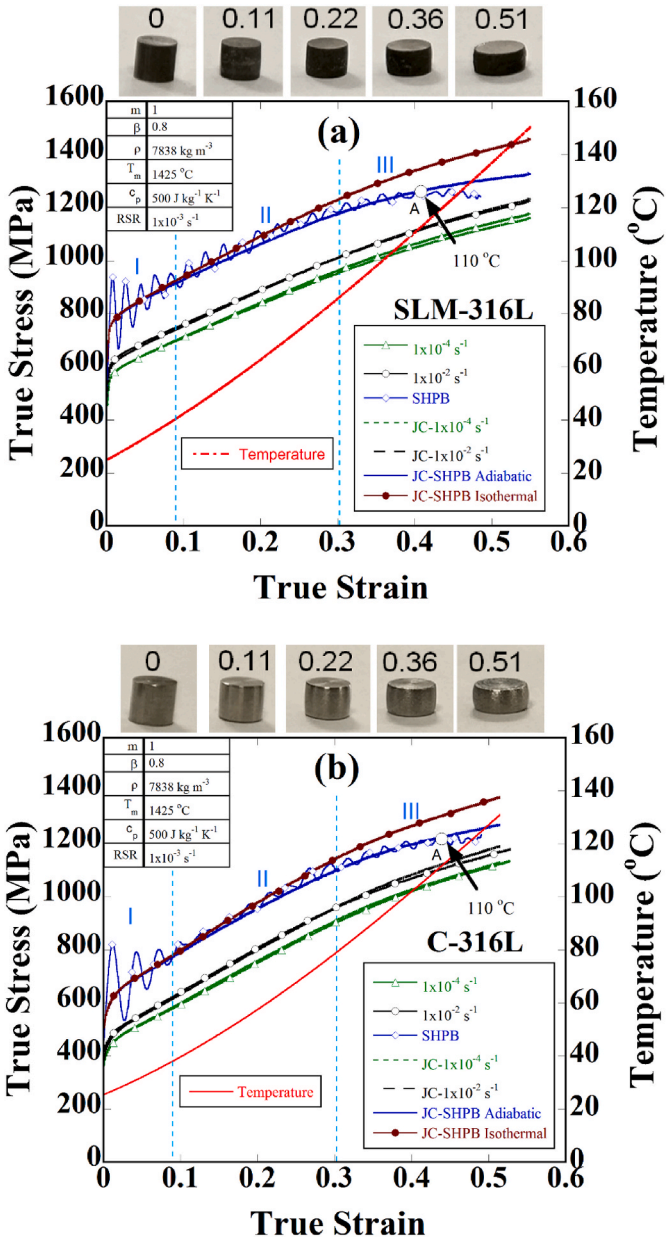

Fig. 9. Adiabatic and isothermal experimental and predicted JC true stress-true strain curves with the predicted adiabatic temperature (a) SLM-316L and (b) C-316L.

calculated isothermal and adiabatic curves in Fig. 10(a) and (b) indicate that adiabatic heating becomes effective after about 0.1 strain. The predicted and experimental SHPB true stress-true strain curves (adiabatic show close agreements with each other until about the point A in the same graphs. After the point A which corresponds to an adiabatic temperature of 110 °C, the experimental stress-strain curves show a reduced work hardening.

Both alloys showed no failure until about 0.51 true strains, as shown in the deformation pictures of the compression tested samples at various strains in Fig. 9(a) and (b). These prove a high ductility of both alloys under compressive loads.

3.4. Microscopy of deformed structures

Microscopic observations of the quasi-statically and dynamically tested specimens revealed a TWIP in SLM-316L, while a martensitic transformation-induced-plasticity in C-316L alloy in a previous study [37]. The quasi-static deformation microstructures of both alloys will be compared in this section with the dynamic deformation microstructures at the same final true strains.

Fig. 10(a–d) show the optical and SEM micrographs of the deformed SLM-316 specimens until about 0.11, 0.22, 0.36 and 0.51 strain, respectively. The parallel twins crossing the melt boundaries are clearly seen in Fig. 10(a and b). A higher twin fraction is found microscopically at 0.11 and 0.22 strains in dynamically tested specimens as compared with the quasi-statically tested specimens given in Ref. [37]. The higher magnification micrographs clearly showed twin planes inside individual grains passing through the melt pools. Furthermore, bent-twins seen in

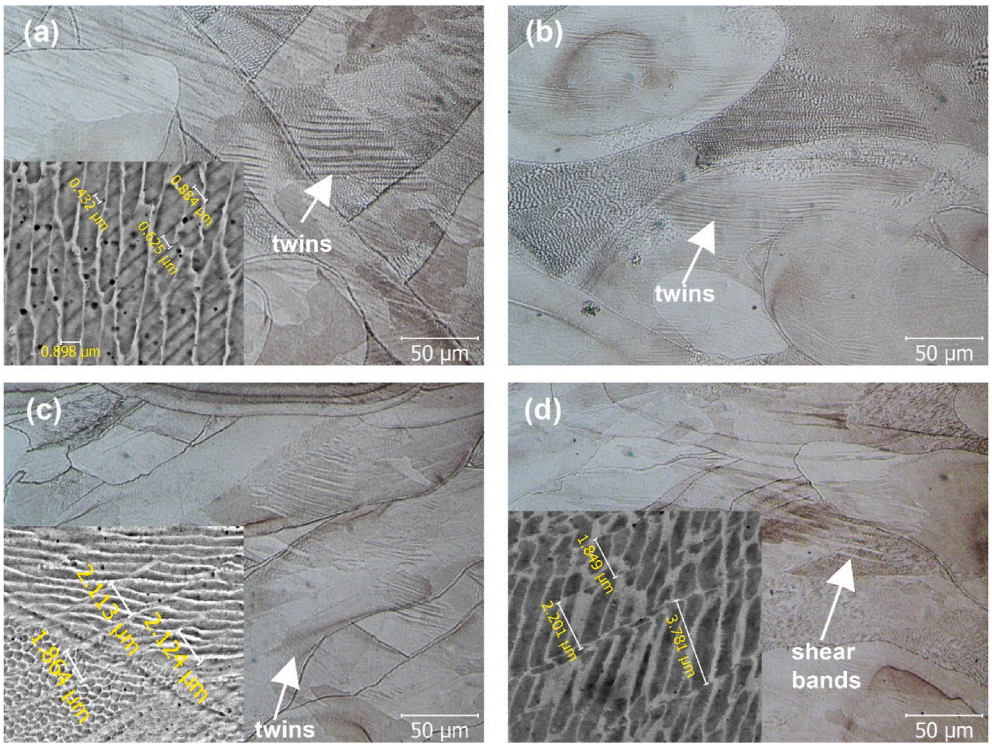

Fig. 10. The optical micrographs showing twinning and shear bands in dynamically tested specimens tested at about (a) 0.11, (b) 0.22, (c) 0.36 and (d) 0.51 strain.

Fig. 10(a) and (b) confirm concurrent plastic deformation via slip by dislocation motion. The distance between twinned regions (containing many twins) was between 1.5 and 2 μm at 0.11 strain, smaller than that of quasi-static tests (6.5–8 μm), while the thickness of twinned regions was almost the same as the quasi-static tests, ~ 1 μm. The distances between individual twins are between 400 and 900 nm and the etch-pits in between the twins are also seen in the dynamically tested samples (shown in the inset of Fig. 10(a)). The sizes of these etch-pits are

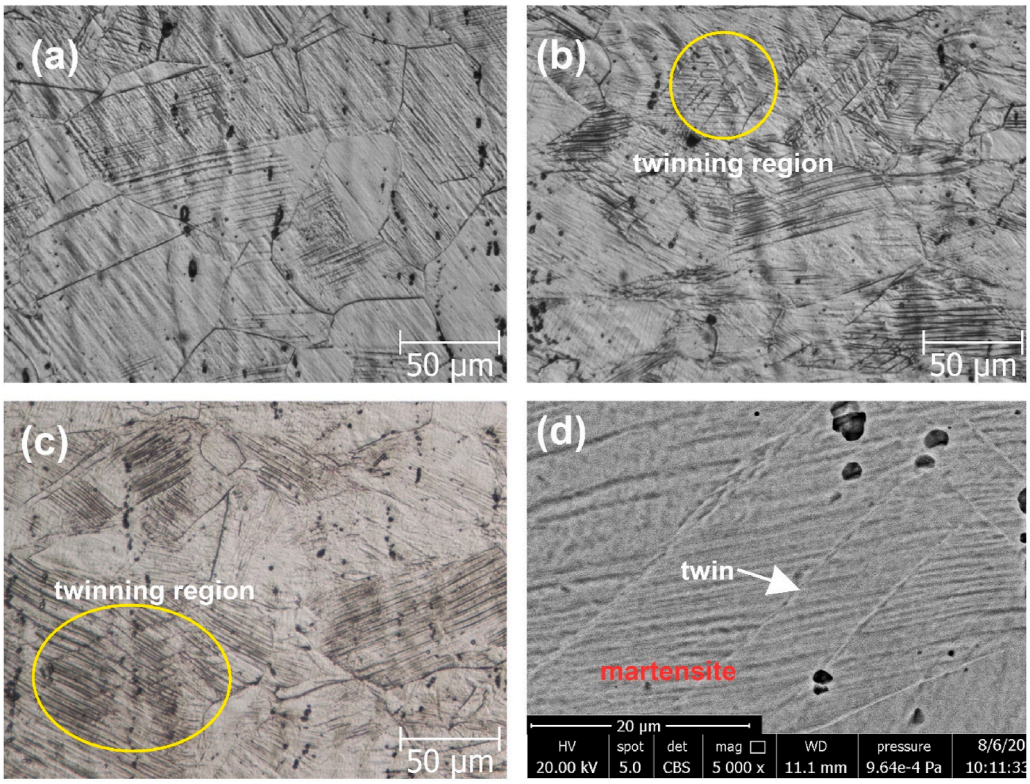

Fig. 11. The optical micrographs showing martensite plates in dynamically tested specimens tested at about (a) 0.11, (b) 0.36 and (c) 0.51 strain and (d) SEM picture of twinning region in (c).

between 100 and 300 nm. On the other side, at increasing strains, at 0.51, adiabatic shear bands are seen, Fig. 10(d). These bands run parallel to each other with a distance between 1.8 and 2.12 μm (shown in the inset of Fig. 10(d)).

Fig. 11(a–c) show the optical and SEM micrographs of the deformed C-316L specimens until about 0.11, 0.36 and 0.51 strain, respectively. A heavy martensite formation is seen at the lowest strain in the dynamically tested specimen, 0.11, (Fig. 11(a), as apposite to the discrete martensite plates seen previously in the quasi-statically tested samples [37]. At higher strains, 0.36 and 0.51, twin formations are also seen (shown by circles in Fig. 11(b) and (c) and by an arrow in Fig. 11(d)).

The XRD spectra of the untested and the dynamically tested specimens of SLM-316L and C-316L shown sequentially in Fig. 12(a) and (b) confirm a fully austenitic phase (γ) in both alloys. The XRD spectra of the dynamically and quasi-statically tested and untested specimens of SLM-316L were found similar. However, the dynamically and quasi-statically tested C-316L specimens exhibited martensite phase α' (110) and α' (211) peaks (Fig. 12(b)). The martensite content was calculated using the α' (110) and γ(111) peaks in Fig. 12(c) for the quasi-statically tested C-316L specimens and in Fig. 12(d) for the dynamically tested C-316L specimens by the Rietveld profile refinement method [50] using a High Score X'pert program. As noted in Fig. 12(d) the relative intensity of α' (110) decreases after 0.22 strain in the dynamically tested specimens. The weight percentages of martensite increase in the quasi-statically tested specimens are almost linear with the strain as seen in Fig. 12 (d). Although the dynamically tested specimens have higher martensite content at low strains, the martensite content remains nearly constant after about 0.22 strain, which also agrees with the microscopic observations in Fig. 11(a–d). After 0.22 strain, the deformation in the dynamically tested specimens is first dominated by twining and slip and then by slip. While, the deformation is dominated by slip at increasing strains in the dynamically tested SLM-316L specimens, which explains a slower decrease in the c values at increasing strains.

4. Discussion

The compression test results revealed a higher flow stress of SLM-316L than C-316L at both quasi-static and high strain rates. As stated earlier in the introduction part, the dislocation density of SLM-316L is reported to be much higher than that of C-316L. The higher dislocation density is generally accounted for the measured higher flow stress of SLM-316L alloy [9].

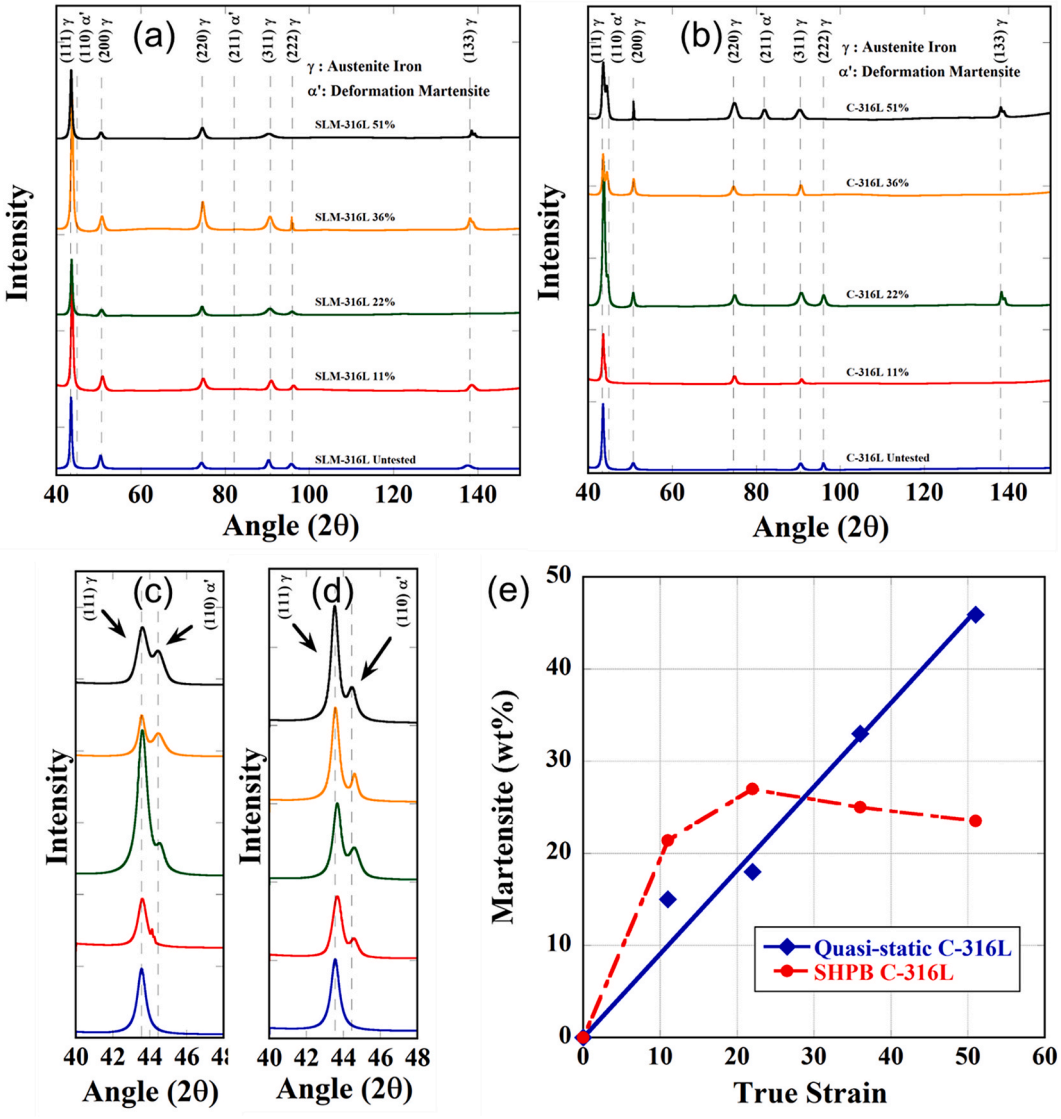

Fig. 12. XRD spectra of dynamically tested (a) SLM-316L and (b) C-316L specimens, (111) peaks of (c) quasi-statically and (d) dynamically tested C-316L specimens and (e) martensite wt% vs. true strain curves of the quasi-statically and dynamically tested C-316L.

The values of c for a C-316L alloy are reported in Ref. [51] between 0.042 and 0.1, which are higher than the c values determined in present study (0.0185 at 0.11 true strain). Eqn. (5) was previously fitted with the experimental tensile yield strengths of an SLM-316L alloy between 10^{-5} and 10^{-1} s^{-1} and the value of m' was reported 0.0248 [35]. Comparably a lower m' value has been recently reported for an LAM deposited 316L within a similar strain rate range, 0.0102 [34]. In the same study, the rate sensitivity parameter of a C-316L alloy was determined 0.0065, which is in contradict with the c values of C-316L alloy listed in Ref. [51] and the m' values determined in present study. The differences in the m' values between present and above studies are most likely due to the difference in the strain rate range studied, the developed microstructure, the sample orientation in SLM and applied test methods (compression and tension). The rate sensitivity parameters reported in Ref. [51] for example were determined between 1000 and 5000 s^{-1}, referring a rate sensitivity parameter in the high strain rate regime. The strain rate sensitivity parameter reported in Ref. [35] was determined under tension in a quasi-static strain rate regime on the specimens which were built horizontally, while the samples in present study were built vertically and tested under compression between quasi-static and high strain rate range. Furthermore, the scanning strategy, as stated earlier, affects the texture formation. In the textured materials, the compression and tension twinning stresses are shown to be different [52]. A higher twinning stress under tension is expected, favoring the deformation by slip [52].

The SLM-316L and C-316L specimens were deformed sequentially by twinning and slip [53] and by the strain induced martensite (α'-martensite) formation and slip [54,55]. The formations of mechanical twins and α'-martensite are influenced by the applied stress and the stacking fault energy (SFE) [56]. The typical range of SFEs of stainless steels was reported, 20–45 mJ m^{-2} for twinning, <20 mJ m^{-2} for martensite and >45 mJ m^{-2} for slip [19]. The stacking faults were proposed to serve for the nucleation of twins [57]. The effective sites for strain-induced martensitic nucleation were proposed to be the intersections of shear bands consisting of ε(hcp) martensite, mechanical twins or dense bundles of stacking faults [54,55,58,59]. Lower is the SFE, larger is the separation between the Shockley partials, which causes a decrease in the extent of cross-slip. Twin planes are considered as the obstacles for the dislocation motion and hence result in a strengthening similar to the Hall-Petch grain size strengthening [56]. As the strain increases, the number of twins formed also increases with a reduction in the distance between twin planes. This comes with a decline in the distance taken by the dislocations and hence an increase in the flow stresses. The strengthening in C-316L is due to the formation of hard martensite plates which is associated with the emissions of high number of dislocations which hardens the austenitic matrix [60]. As with slip, twining and also martensite occur when the applied shear stress is greater than a critical stress on a highly stressed plane [61]. The twinning stress was shown to have a weak or no dependency on temperature [59] and strain rate [44]. The increased work hardening rates of the dynamically tested SLM-316L and C-316L in the initial part of Region II in Fig. 6, where the adiabatic heating is lower, tend to conclude that the twin and martensite fractions increase at increasing strain rates. The increased martensite fraction at low strains of high strain rate tests was also reported previously for a 304 stainless steel. Martensite formation was found higher at 10^{3} s^{-1} than at 10^{-3} s^{-1} until about 0.25 strain [62,63]. The reduced work hardening rate of the dynamically tested specimens in the Region II and Region III is due to the adiabatic heating of the specimens. The temperature rise due to adiabatic heating, as stated in previous works in a 304 stainless steel [64–67], reduces the driving force for the martensite transformation. The fraction of twin formation is also expected to decline with increasing temperature. The reduced work hardening of experimental stress-strain curves after the point A in Fig. 6 is further attributed to a decrease in the m value after about 100 °C which is also reported for 316L and 316LN alloys in Ref. [68].

The deformation by dislocation glide is governed by the thermally activated deformation mechanism [69]. The Thermally activated deformation stress (σ) is given by the following relation [70,71].

$$\sigma = \frac{M(\Delta G_o - kTln\dot{\varepsilon}_o)}{V^*} + \frac{MkT}{V^*} ln\dot{\varepsilon} = \sigma_i + k_1 ln\dot{\varepsilon} \quad (9)$$

In Eqn. (9), ΔG_o is the activation free energy, M is the Taylor's factor (~3), k is the Boltzmann's constant, V^* is the activation volume and k_1 is the slope of $\sigma - ln\varepsilon$ curve, $k_1 = \left(\frac{\partial\sigma}{\partial ln\dot{\varepsilon}}\right)_{T,\varepsilon} = \frac{MkT}{V^*}$. The strain rate sensitivity is inversely proportional to the activation volume. The calculated activation volumes of the tested SLM-316L and C-316L are tabulated in Table 2 at different strains and different strain rate range (between $1x10^{-4}$ and $1x10^{-2}$ s^{-1} and between $1x10^{-4}$ and 2500-2800 s^{-1}). In the quasi-static strain rate range, the activation volumes of SLM-316L are lower than those of C-316L and the activation volumes decrease as the strain increases from 0.11 to 0.22 strain. A similar trend is also seen in the apparent activation volumes, V_a ($MkT\frac{\Delta ln\dot{\varepsilon}}{\Delta\sigma}$), of both alloys as tabulated together with the corresponding m' values in Table 2. In the quasi-static-high strain rate range, the activation volumes of both alloys become very much similar. The activation volume of SLM-316L between two strain rate ranges are pretty similar, while the activation volume of C-316L is slightly reduced in the quasi-static-high strain rate range. The activation volumes of both alloys are in the range of 100 b^3 (where b is the Burgers' vector, 0.255 nm [72]), corresponding to dislocation intersections [70]. The similar strain rate sensitivity of C-316L indicates a similar thermally activated deformation process (slip by dislocation) involvement in both alloys.

5. Conclusions

The strain rate dependent compressive flow stresses of a SLM-316L alloy and a C-316L alloy having similar grain sizes were determined, for comparison, between $1x10^{-4}$ and ~2500 s^{-1} and between $1x10^{-4}$ and ~2800 s^{-1}, respectively. The JC material model parameters were also determined for both alloys for the adiabatic and isothermal condition. The microstructural examinations of the cross-sections of deformed specimens exhibited a twinning-induced-plasticity in SLM-316L and a martensitic transformation-induced-plasticity in C-316L alloy at both quasi-static and high strain rates. In the dynamically tested specimens, higher fractions of martensite and twin formation were detected microscopically until about 0.22 strain. XRD measurements also confirmed the higher fractions of martensite formation in the dynamically tested C-316L specimens until about 0.22 strain. While, the adiabatic heating of the dynamically tested specimens decreased the twin

Table 2
The deformation activation volumes in two different strain rate ranges.

Specimen/ strain	Strain rate range	$\frac{MkT}{V^*}$ (MPa s^{-1})	V^* (nm^3)	V^*b^3	m'	V_ab^3
C-316L 0.11	$1x10^{-4}$-$1x10^{-2}$ s^{-1}	8.03	1.54	92.7	0.0131	92.6
C-316L 0.22	$1x10^{-4}$-$1x10^{-2}$ s^{-1}	9.98	1.24	74.6	0.0129	83.2
SLM-316L 0.11	$1x10^{-4}$-$1x10^{-2}$ s^{-1}	12.59	0.98	59.1	0.0166	62.3
SLM-316L 0.22	$1x10^{-4}$-$1x10^{-2}$ s^{-1}	15.20	0.81	48.9	0.0177	49.0
C-316L 0.11	$1x10^{-4}$-2800 s^{-1}	11.42	1.08	65.2	0.0164	63.8
C-316L 0.22	$1x10^{-4}$-2800 s^{-1}	11.97	1.03	62.2	0.0139	62.3
SLM-316L 0.11	$1x10^{-4}$-2500 s^{-1}	12.62	0.98	59.0	0.0151	58.6
SLM-316L 0.22	$1x10^{-4}$-2500 s^{-1}	14.15	0.87	52.6	0.0147	53.2

and martensite formation at higher strains. The rate sensitivity of SLM-316L was determined to be slightly higher in the quasi-static strain rate range, while the rate sensitivities of both alloys were determined to be similar in the quasi-static-high strain rate range at 0.11 strain. A more rapid decline at increasing strains in the rate sensitivity of C-316L was found in the quasi-static-high strain rate range. The activation volumes of SLM-316L between two strain-rate ranges were determined to be similar, while the activation volume of C-316L was slightly reduced in the quasi-static-high strain rate range. The activation volumes of both alloys, corresponding to dislocation intersections, indicated a similar thermally activated deformation process (slip by dislocation) involvement in both alloys.

Data availability

The data presented in present study are parts of an ongoing study; therefore, the raw/processed data cannot be shared at this time.

CRediT authorship contribution statement

Mustafa Güden: Formal analysis, Conceptualization, Writing – review & editing, Supervision. **Samed Enser:** Investigation, Formal analysis. **Mesut Bayhan:** Investigation, Formal analysis. **Alper Taşdemirci:** Conceptualization, Writing – review & editing. **Hakan Yavaş:** Conceptualization, Writing – review & editing.

Declaration of competing interest

The authors declare that they have no known competing financial interests or personal relationships that could have appeared to influence the work reported in this paper.

References

[1] K. Saeidi, X. Gao, Y. Zhong, Z.J. Shen, Hardened austenite steel with columnar sub-grain structure formed by laser melting, Mater. Sci. Eng. A-Struct. Mater. Prop. Microstruct. Process. 625 (2015) 221–229.

[2] B. Song, X. Zhao, S. Li, C. Han, Q. Wei, S. Wen, J. Liu, Y. Shi, Differences in microstructure and properties between selective laser melting and traditional manufacturing for fabrication of metal parts: a review, Front. Mech. Eng. 10 (2) (2015) 111–125.

[3] Y. Zhong, L.F. Liu, S. Wikman, D.Q. Cui, Z.J. Shen, Intragranular cellular segregation network structure strengthening 316L stainless steel prepared by selective laser melting, J. Nucl. Mater. 470 (2016) 170–178.

[4] M. Zietala, T. Durejko, M. Polanski, I. Kunce, T. Plocinski, W. Zielinski, M. Lazinska, W. Stepniowski, T. Czujko, K.J. Kurzydlowski, Z. Bojar, The microstructure, mechanical properties and corrosion resistance of 316 L stainless steel fabricated using laser engineered net shaping, Mater. Sci. Eng. A-Struct. Mater. Prop. Microstruct. Process. 677 (2016) 1–10.

[5] S. Gorsse, C. Hutchinson, M. Goune, R. Banerjee, Additive manufacturing of metals: a brief review of the characteristic microstructures and properties of steels, Ti-6Al-4V and high-entropy alloys, Sci. Technol. Adv. Mater. 18 (1) (2017) 584–610.

[6] M.-S. Pham, P. Hooper, Roles of microstructures on deformation response of 316 stainless steel made by 3D printing, in: AIP Conference Proceedings, vol. 1896, 2017, 040017, 1.

[7] M.S. Pham, B. Dovgyy, P.A. Hooper, Twinning induced plasticity in austenitic stainless steel 316L made by additive manufacturing, Mater. Sci. Eng. A-Struct. Mater. Prop. Microstruct. Process. 704 (2017) 102–111.

[8] Y.M. Wang, T. Voisin, J.T. McKeown, J. Ye, N.P. Calta, Z. Li, Z. Zeng, Y. Zhang, W. Chen, T.T. Roehling, R.T. Ott, M.K. Santala, Philip J. Depond, M.J. Matthews, A. V. Hamza, T. Zhu, Additively manufactured hierarchical stainless steels with high strength and ductility, Medium: X; Size (2017) 63–71.

[9] Y.J. Yin, J.Q. Sun, J. Guo, X.F. Kan, D.C. Yang, Mechanism of high yield strength and yield ratio of 316 L stainless steel by additive manufacturing, Mater. Sci. Eng. A-Struct. Mater. Prop. Microstruct. Process. 744 (2019) 773–777.

[10] X.L. Wang, J.A. Muniz-Lerma, M.A. Shandiz, O. Sanchez-Mata, M. Brochu, Crystallographic-orientation-dependent tensile behaviours of stainless steel 316L fabricated by laser powder bed fusion, Mater. Sci. Eng. A-Struct. Mater. Prop. Microstruct. Process. 766 (2019) 16.

[11] M.M. Ma, Z.M. Wang, X.Y. Zeng, A comparison on metallurgical behaviors of 316L stainless steel by selective laser melting and laser cladding deposition, Mater. Sci. Eng. A-Struct. Mater. Prop. Microstruct. Process. 685 (2017) 265–273.

[12] L.F. Liu, Q.Q. Ding, Y. Zhong, J. Zou, J. Wu, Y.L. Chiu, J.X. Li, Z. Zhang, Q. Yu, Z. J. Shen, Dislocation network in additive manufactured steel breaks strength-ductility trade-off, Mater. Today 21 (4) (2018) 354–361.

[13] Z. Sun, X. Tan, S.B. Tor, C.K. Chua, Simultaneously enhanced strength and ductility for 3D-printed stainless steel 316L by selective laser melting, NPG Asia Mater. 10 (4) (2018) 127–136.

[14] S.-H. Sun, T. Ishimoto, K. Hagihara, Y. Tsutsumi, T. Hanawa, T. Nakano, Excellent mechanical and corrosion properties of austenitic stainless steel with a unique crystallographic lamellar microstructure via selective laser melting, Scripta Mater. 159 (2019) 89–93.

[15] T. Niendorf, S. Leuders, A. Riemer, F. Brenne, T. Tröster, H.A. Richard, D. Schwarze, Functionally graded alloys obtained by additive manufacturing, Adv. Eng. Mater. 16 (7) (2014) 857–861.

[16] O. Andreau, I. Koutiri, P. Peyre, J.-D. Penot, N. Saintier, E. Pessard, T. De Terris, C. Dupuy, T. Baudin, Texture control of 316L parts by modulation of the melt pool morphology in selective laser melting, J. Mater. Process. Technol. 264 (2019) 21–31.

[17] T. Niendorf, S. Leuders, A. Riemer, H.A. Richard, T. Tröster, D. Schwarze, Highly anisotropic steel processed by selective laser melting, Metall. Mater. Trans. B 44 (4) (2013) 794–796.

[18] J.J. Marattukalam, D. Karlsson, V. Pacheco, P. Beran, U. Wiklund, U. Jansson, B. Hjorvarsson, M. Sahlberg, The effect of laser scanning strategies on texture, mechanical properties, and site-specific grain orientation in selective laser melted 316L SS, Mater. Des. 193 (2020) 11.

[19] W. Woo, J.S. Jeong, D.K. Kim, C.M. Lee, S.H. Choi, J.Y. Suh, S.Y. Lee, S. Harjo, T. Kawasaki, Stacking fault energy analyses of additively manufactured stainless steel 316L and CrCoNi medium entropy alloy using in situ neutron diffraction, Sci. Rep. 10 (1) (2020) 15.

[20] A. Rottger, K. Geenen, M. Windmann, F. Binner, W. Theisen, Comparison of microstructure and mechanical properties of 316 L austenitic steel processed by selective laser melting with hot-isostatic pressed and cast material, Mater. Sci. Eng. A-Struct. Mater. Prop. Microstruct. Process. 678 (2016) 365–376.

[21] N. Haghdadi, M. Laleh, M. Moyle, S. Primig, Additive manufacturing of steels: a review of achievements and challenges, J. Mater. Sci. 56 (1) (2021) 64–107.

[22] M. Güden, H. Yavaş, A.A. Tanrıkulu, A. Taşdemirci, B. Akın, S. Enser, A. Karakuş, B.A. Hamat, Orientation dependent tensile properties of a selective-laser-melt 316L stainless steel, Mater. Sci. Eng., A 824 (2021) 141808.

[23] M. Shamsujjoha, S.R. Agnew, J.M. Fitz-Gerald, W.R. Moore, T.A. Newman, High strength and ductility of additively manufactured 316L stainless steel explained, Metall. Mater. Trans. A-Phys. Metall. Mater. Sci. 49A (7) (2018) 3011–3027.

[24] A.M. Eleiche, C. Albertini, M. Montagnani, The influence OF strain-rate history ON the ambient tensile-strength OF AISI TYPE-316 stainless-steel, Nucl. Eng. Des. 88 (2) (1985) 131–141.

[25] G.S. Langdon, G.K. Schleyer, Unusual Strain Rate Sensitive Behaviour of AISI 316L Austenitic Stainless Steel, vol. 39, 2004, pp. 71–86, 1.

[26] Q. Xue, G.T. Gray, Development of adiabatic shear bands in annealed 316L stainless steel: Part I. Correlation between evolving microstructure and mechanical behavior, Metall. Mater. Trans. 37 (8) (2006) 2435–2446.

[27] Q. Xue, E.K. Cerreta, G.T. Gray, Microstructural characteristics of post-shear localization in cold-rolled 316L stainless steel, Acta Mater. 55 (2) (2007) 691–704.

[28] W.-S. Lee, C.-F. Lin, T.-J. Liu, Strain rate dependence of impact properties of sintered 316L stainless steel, J. Nucl. Mater. 359 (3) (2006) 247–257.

[29] W.-S. Lee, T.-H. Chen, C.-F. Lin, W.-Z. Luo, Dynamic mechanical response of biomedical 316L stainless steel as function of strain rate and temperature, J Bioinorg. Chem. Appl. 2011 (2011) 13.

[30] W.-S. Lee, C.-F. Lin, T.-H. Chen, W.-Z. Luo, High temperature deformation and fracture behaviour of 316L stainless steel under high strain rate loading, J. Nucl. Mater. 420 (1) (2012) 226–234.

[31] S. Acharya, A. Moitra, S. Bysakh, M. Nanibabu, S.A. Krishanan, C. K. Mukhopadhyay, K.V. Rajkumar, G. Sasikala, A.K. Mukhopadhyay, D.K. Mondal, K.S. Ghosh, K. Muraleedharan, Effect of High Strain Rate Deformation on the Properties of SS304L and SS316LN Alloys, Mechanics of Materials, 2019, p. 103073.

[32] J. Peng, J. Peng, K.S. Li, J.F. Pei, C.Y. Zhou, Temperature-dependent SRS behavior of 316L and its constitutive model, Acta Metall. Sin.-Engl. Lett. 31 (3) (2018) 234–244.

[33] Y.Z. Li, M.X. Huang, Carbon-dislocation interaction-induced abnormal strain-rate sensitivity in twinning-induced plasticity steels, Metall. Mater. Trans. A-Phys. Metall. Mater. Sci. 50A (6) (2019) 2570–2575.

[34] F. Khodabakhshi, M.H. Farshidianfar, A.P. Gerlich, M. Nosko, V. Trembošová, A. Khajepour, Microstructure, strain-rate sensitivity, work hardening, and fracture behavior of laser additive manufactured austenitic and martensitic stainless steel structures, Mater. Sci. Eng., A 756 (2019) 545–561.

[35] Z. Li, T. Voisin, J.T. McKeown, J.C. Ye, T. Braun, C. Kamath, W.E. King, Y.M. Wang, Tensile properties, strain rate sensitivity, and activation volume of additively manufactured 316L stainless steels, Int. J. Plast. 120 (2019) 395–410.

[36] T.J. Kneen, C. Barrett, G.P. Manogharan, P.R. Carlson, J. Dimon, B.P. Conner, Mechanical behaviour and high strain rate deformation of stainless steel 316L processed by selective laser melting, Int. J. Rapid Manuf. 9 (9) (2020) 84–102.

[37] S. Enser, H. Yavas, B.A. Hamat, H. Aydın, G. Kafadar, A.A. Tanrıkulu, H.Z. Kazdal, F. Ozturk, M. Güden, Comparing compression deformation and rate sensitivity of additively manufactured and extruded-annealed 316L alloys, J. Mater. Eng. Perform. (2021).

[38] O.O. Salman, F. Brenne, T. Niendorf, J. Eckert, K.G. Prashanth, T. He, S. Scudino, Impact of the scanning strategy on the mechanical behavior of 316L steel synthesized by selective laser melting, J. Manuf. Process. 45 (2019) 255–261.

[39] D.J. Frew, M.J. Forrestal, W. Chen, Pulse shaping techniques for testing brittle materials with a split Hopkinson pressure bar, Exp. Mech. 42 (1) (2002) 93–106.

[40] M.R. Khosravani, K. Weinberg, A review on split Hopkinson bar experiments on the dynamic characterisation of concrete, Construct. Build. Mater. 190 (2018) 1264–1283.
[41] E.D.H. Davies, S.C. Hunter, The dynamic compression testing of solids by the method of the split Hopkinson pressure bar, J. Mech. Phys. Solid. 11 (3) (1963) 155–179.
[42] H. Kolsky, An investigation of the mechanical properties of materials at very high rates of loading, Proc. Phys. Soc. B 62 (11) (1949) 676.
[43] G.R. Johnson, W.H. C, A Constitutive Model and Data for Metals Subjected to Large Strains, High Strain Rates and High Temperatures Proceedings of the 7th International Symposium on Ballistics, The Hague, The Netherlands, 1983, p. 541.
[44] M.A. Meyers, K.K. Chawla, Mechanical Behavior of Materials, Cambridge University Press, 2009.
[45] G.-S. Ham, S.-H. Park, K.-A. Lee, Room and elevated temperature compressive deformation behavior of AISI 316L alloy fabricated by selective laser melting process, Korean J. Met. Mater. 57 (5) (2019) 295–303.
[46] G.I. Taylor, H. Quinney, The Latent Energy Remaining in a Metal after Cold Working 143, 1934, pp. 307–326, 849.
[47] K.G. Samuel, S.L. Mannan, V.M. Radhakrishnan, The influence of temperature and prior cold work on the strain-hardening parameters of a type 316 LN stainless steel, Int. J. Pres. Ves. Pip. 52 (2) (1992) 151–157.
[48] N.I. Vazquez-Fernandez, G.C. Soares, J.L. Smith, J.D. Seidt, M. Isakov, A. Gilat, V. T. Kuokkala, M. Hokka, Adiabatic heating of austenitic stainless steels at different strain rates, J. Dynam. Behav. Mater. 5 (3) (2019) 221–229.
[49] D. Rittel, L.H. Zhang, S. Osovski, The dependence of the Taylor–Quinney coefficient on the dynamic loading mode, J. Mech. Phys. Solid. 107 (2017) 96–114.
[50] D.L. Bish, S.A. Howard, Quantitative phase analysis using the Rietveld method, J. Appl. Crystallogr. 21 (2) (1988) 86–91.
[51] N.E. Karkalos, A.P. Markopoulos, Determination of Johnson-Cook material model parameters by an optimization approach using the fireworks algorithm, Procedia Manuf. 22 (2018) 107–113.
[52] J.W. Christian, S. Mahajan, Deformation twinning, Prog. Mater. Sci. 39 (1–2) (1995) 1–157.
[53] R.A. Hadfield, Some newly discovered properties of iron and manganese, in: Minutes of the Proceedings of the Institution of Civil Engineers 93, 1888, pp. 61–75, 1888.
[54] R. Lagneborgj, The martensite transformation in 18% Cr-8% Ni steels, Acta Metall. 12 (7) (1964) 823–843.
[55] J.A. Venables, The martensite transformation in stainless steel, Philos. Mag.: J. Theor. Exp. Appl. Phys. 7 (73) (1962) 35–44.
[56] L. Rémy, A. Pineau, Twinning and strain-induced f.c.c. → h.c.p. transformation on the mechanical properties of Co-Ni-Cr-Mo alloys, Mater. Sci. Eng. 26 (1) (1976) 123–132.
[57] H. Idrissi, K. Renard, L. Ryelandt, D. Schryvers, P.J. Jacques, On the mechanism of twin formation in Fe–Mn–C TWIP steels, Acta Mater. 58 (7) (2010) 2464–2476.
[58] G.B. Olson, M. Cohen, Kinetics of strain-induced martensitic nucleation, Metall. Trans. A 6 (4) (1975) 791–795.
[59] S. Mahajan, D.F. Williams, Deformation twinning in metals and alloys, Int. Metall. Rev. 18 (2) (1973) 43–61.
[60] J. Liu, C. Chen, Q. Feng, X. Fang, H. Wang, F. Liu, J. Lu, D. Raabe, Dislocation activities at the martensite phase transformation interface in metastable austenitic stainless steel: an in-situ TEM study, Mater. Sci. Eng., A 703 (2017) 236–243.
[61] J.A. Venables, Deformation twinning in face-centred cubic metals, Philos. Mag.: J. Theor. Exp. Appl. Phys. 6 (63) (1961) 379–396.
[62] S.S. Hecker, M.G. Stout, K.P. Staudhammer, J.L. Smith, Effects of strain state and strain rate on deformation-induced transformation in 304 stainless steel: Part I. Magnetic measurements and mechanical behavior, Metall. Trans. A 13 (4) (1982) 619–626.
[63] L.E. Murr, K.P. Staudhammer, S.S. Hecker, Effects of strain state and strain rate on deformation-induced transformation in 304 stainless steel: Part II. Microstructural study, Metall. Trans. A 13 (4) (1982) 627–635.
[64] G.L. Huang, D. Matlock, G. Krauss, Martensite formation, strain rate sensitivity, and deformation behavior of type 304 stainless steel sheet, Metall. Trans. A 20 (7) (1989) 1239–1246.
[65] M. Isakov, S. Hiermaier, V.-T. Kuokkala, Effect of strain rate on the martensitic transformation during plastic deformation of an austenitic stainless steel, Metall. Mater. Trans. 46 (6) (2015) 2352–2355.
[66] J. Talonen, H. Hänninen, Formation of shear bands and strain-induced martensite during plastic deformation of metastable austenitic stainless steels, Acta Mater. 55 (18) (2007) 6108–6118.
[67] S. Sunil, R. Kapoor, Effect of strain rate on the formation of strain-induced martensite in AISI 304L stainless steel, Metall. Mater. Trans. 51 (11) (2020) 5667–5676.
[68] T.S. Byun, N. Hashimoto, K. Farrell, Temperature dependence of strain hardening and plastic instability behaviors in austenitic stainless steels, Acta Mater. 52 (13) (2004) 3889–3899.
[69] H. Conrad, H. Wiedersich, Activation energy for deformation of metals at low temperatures, Acta Metall. 8 (2) (1960) 128–130.
[70] H. Conrad, Thermally activated deformation of metals, J. Occup. Med. 16 (7) (1964) 582–588.
[71] U.F. Kocks, A.S. Argon, M.F. Ashby, B. Chalmers, J.W. Christian, T.B. Massalski, Progress in Materials Science, vol. 19, Pergamon, Oxford, 1975 (etc.).
[72] G.K. Williamson, R.E. Smallman III., Dislocation densities in some annealed and cold-worked metals from measurements on the X-ray debye-scherrer spectrum, Philos. Mag.: J. Theor. Exp. Appl. Phys. 1 (1) (1956) 34–46.